# Investigation on Miage/Brenva Glaciers in The Alps From 50s to-date Based on Remote-Sensing Data

Rasoul Eskandari [1], Nicola Genzano [1], Davide Fugazza [2], Marco Scaioni [1]
[1] Politecnico di Milano, Dept. of Architecture, Built Environment and Construction Engineering (DABC)
via Ponzio 31, 20133 Milano, Italy – email: [rasoul.eskandari, nicola.genzano, marco.scaioni]@polimi.it
[2] Università degli Studi di Milano, Department of Environmental Science and Policy (DESP), Via Celoria 2, 20133 Milano, Italy
email: davide.fugazza@unimi.it

**Key Words:** Aerial Photo Archives, European Ground Motion Service, Ground Control, Monitoring, Multi-temporal, Structure-from-Motion

**Abstract:**

The Miage and Brenva Glaciers in Mount Blanc Massif (Italy) are two of the major glaciers in the Alps. To assess the evolution of these glaciers, we use multiple data sources from remote sensing, and we adopt different techniques to extract important information on their conditions during a long period (i.e., ~60 years). The first approach, which is based on the use of aerial photos and satellite imagery (SPOT 6), allows assessing the volume change of Miage Glacier over the period 1952-2014. The second approach, which is based on the use of optical satellite observations such as Landsat 5/8/9 and Sentinel 2, aims to evaluate the spatial variability and the temporal trends of the snow cover of both glaciers from 1984 up to now. The achieved results, that are coherent with the ones reported by the scientific literature, show that volumetric changes of Miage Glacier underwent a period of gain between 1975-1991, followed by an impressive decay phase. Concerning the snow cover analysis, our findings highlight that for both glaciers the area covered by snow reduces persistently year-by-year, especially in the case of the Miage Glacier.

## 1. Introduction

Remote sensing data have become a powerful tool for investigating the evolution of Alpine glaciers, which have impressively suffered from the effects of climate change during the latest decades (Racoviteanu et al, 2008; Taylor et al., 2021). Remote sensing data offers multiple advantages: large ground coverage, independence from accessing harsh environments such as in high mountain areas, capability of collecting multiple types of information.

The Miage and Brenva Glaciers are two large glaciers in the Alps, covering an extension of 10.09 km$^2$ and 5.95 km$^2$, respectively (Paul et al., 2020), see Figure 1. In some previous papers, some datasets of aerial photos retrieved from an online archive were used to reconstruct point clouds at different epochs for computing volume change. As reported in Scaioni et al. (2023), a technique called *Multitemporal Structure-from-Motion* (MSfM) was applied to cope with the poor ground control in the region. Six aerial datasets collected from 1967 to 2006 using different types of cameras (analogue/digital) and radiometric content (panchromatic/RGB) were processed, obtaining final registration errors in the range of 1 m.

In this paper the previous study has been extended by including other data sets and new methodological solutions (see Sect. 2) to overcome some open issues. In addition, a new type of investigation has been applied to the study area. On the basis of optical satellite observations, we investigated the seasonal and inter-annual evolution of the snow-cover of these glaciers. Indeed, by defining a multi-temporal approach, we analysed the time-series of medium-high spatial resolution satellite observations, such as Landsat 5/8/9 and Sentinel 2. Here, we present and discuss the proposed approach, by showing the results achieved on Miage and Brenva glaciers during the period 1984-2023 (more details in Section 3).

We thus aim to show two different techniques which can be used to extract important information over glaciers over long time scales, i.e. the 50s for MSfM with archive aerial imagery and the 80s for snow cover analysis based on optical satellite observations.

## 2. Photogrammetric point-cloud analysis

### 2.1 Photogrammetric datasets

In this paper a larger number of aerial blocks were retrieved from national online archives from France (“IGN – Remontez le temps;” see IGNF, 2024) and Switzerland (LUISS, see SwissTopo, 2024). The time coverage spans over sixty years from 1952 to 2006. Additional datasets were also available (e.g., in 2012) but they did not provide the coverage of the main surface of both glaciers. In addition, a SPOT 6 high–resolution satellite stereo pair acquired by CNES on 14/09/2014 was used to reconstruct the glacier after 2012. SPOT6 carries an instrument with a panchromatic band at 1.5 m GSD and four multispectral bands at 6 m GSD, respectively. Main properties of the adopted images are reported in Table 1.

### 2.2 Ground control

Ground control is necessary to establish a geodetic *datum* for georeferencing multitemporal data and to allow the comparison of point clouds for change detection purpose (Lindenbergh and Pietrzyk, 2015). When working with data sets from the abovementioned archives, ground control points (GCPs) are not available and direct georeferencing was not adopted. In addition, seeking and measuring GCPs in multiple epoch imagery covering high-mountain areas is quite difficult, if not impossible.

In this research two solutions have been considered to establish the geodetic datum: (1) the measurement on the field of GCPs based on differential GNSS techniques; (2) the use of MSfM to register together photogrammetric datasets made up of aerial images (see Subsect. 2.3). Solution (1) was excluded since the identification of GCPs in multiple epochs would be impossible. Consequently, the focus was put on the application of MSfM, as presented in the following subsection.

### 2.3 *Multitemporal Structure-from-Motion* (MSfM)

**2.3.1 Background on MSfM.** *Structure-from-Motion* (SfM) is referred today as the entire automatic procedure for computing the image orientation of a block of images (James et al., 2019).

| Acquisition time | Data provider | #Images (type) | Camera Model (focal length – [mm]) | Avg. flying altitude [m a.s.l.] | Image format | Image size [Mpixels] | Avg. pixelsize [µm] / GSD [cm] |
|---|---|---|---|---|---|---|---|
| **1952** (27 Jul) | IGNF | 32 (PAN) | unknown | 6700 – 8000 | unknown | 29.6 | 21 / 170 |
| **1956** (25 Jul) | LUISS | 11 (PAN) | Leica RC5 (115.34) | 5,300 | 18 x 18 cm | 80.5 | 20 / 66 |
| **1958** | IGNF | 20 (PAN) | unknown | 7500 | unknown | 77.8 | 21 / 90 |
| **1967** (Oct 11-12) | IGNF | 23 (PAN) | Leica RC10 (150) | 6,350 | 23 x 23 cm | 29.1 | 21 /100 |
| **1979** (Sept 5) | IGNF | 19 (PAN) | Leica RC10 (150) | 5,700 | 23 x 23 cm | 137.0 | 21 / 68 |
| **1983** (26 Sept) | IGNF | 13 (PAN) | Leica RC20 (150) | 6,700-8000 | 23 x 23 cm | 13622 | 21 / 76 |
| **1988** (Jul 26) | IGNF | 23 (PAN) | Leica RC10 (152.06) | 6,150 | 23 x 23 cm | 135.8 | 21 /74 |
| **1996** (Jul 31-Aug 4) | IGNF | 26 (RGB) | Zeiss RMKTOP15 (153.47) | 5,020 | 23 x 23 cm | 80.9 | 28 / 77 |
| **2000** (Jun 26-Aug 1) | IGNF | 24 (PAN) | Zeiss RMKTOP15 (152.76) | 5,540 | 23 x 23 cm | 75.6 | 28 / 90 |
| **2001** (Aug 1-13) | IGNF | 73 (RGB) | Zeiss RMKTOP15 (153.02) | 4,780 | 23 x 23 cm | 60.4 | 28 / 76 |
| **2004** | IGNF | 56 (RGB) | Zeiss RMKTOP30 (150) | 2,300 – 5,400 | 23 x 23 cm | 85.7 | 28 / 58 |
| **2006** (Aug 23-Sept 5) | IGNF | 78 (RGB) | DAC IGNF (59.94) | 7,300 – 9,000 | 4,096 x 4,096 pix | 16.8 | 9 / 100 |

Table 1. Properties of photogrammetric datasets from online repositories (DAC: digital aerial camera; PAN: panchromatic photos; RGB: colour photos). The average ground sampling distance (GSD) is given in correspondence of the Miage Glacier tongue.

A block is processed independently form others and georeferenced by means of ground control. This is generally presented by means of GCPs, though the diffusion of direct-georeferencing (now also possible with small commercial drones – see Elias et al., 2024) can be exploited to this aim. After Multi-View-Stereo (MVS) dense matching, a point cloud is obtained to be compared with respect to other datasets. Feurer and Vinatier (2018) proposed to bundle together multitemporal blocks and to compute the image orientation at the same time (‘Time-SIFT’). The advantage of this approach is that images from all epochs are aligned together based on tie points extracted across images in each photogrammetric block and across different multitemporal blocks. Ground control is provided by GCPs to be used only for global georeferencing, requiring a quality that may also be at lower accuracy.

The implementation proposed in this paper is termed *Multitemporal SfM* (MSfM) and is based on a popular, low-cost software package (Agisoft Metashape Professional ver. 2.1.1 – AMP; www.agisoft.com) that does not require tailored code development (see Genzano et al., 2024). MSfM consists of four main steps:

1. independent SfM per each data set with computation of “free-net” BBA including camera self-calibration;
2. multiple blocks are transformed into the same reference system based on a minimum set of common GCPs;
3. tie points are extracted from all blocks at different epochs;
4. a common BBA including all tie points and GCPs is computed to estimate the final exterior orientation (EO) parameters per each image; and
5. the EO computed per each epoch is constrained to compute a corresponding *dense point cloud* (DPC) based on MVS matching implemented in AMP.

A final empirical quality assessment is based on the comparison of segmented point clouds inside some well distributed and representative Stable Areas (SAs), see Subsect. 2.4.

**2.3.2 Modified processing workflow.** The pipeline described above has been demonstrated to work effectively with different types of aerial photos, including the ones from archives (Scaioni et al., 2023; Genzano et al., 2024). On the other hand, some experiments on the large dataset described at the beginning of this section and spanning over 48 years, results in the definition of a specific operational workflow. The main characteristics of the modified processing pipeline are as follows:

1. no image pre-processing and masking for analogue photos was applied as reported in previous papers, where only a few epochs were exploited. The choice is motivated by the purpose of speeding up the full process;
2. MSfM is applied to each pair of consecutive epochs, to obtain a series of good relative alignments; consequently, relative changes occurred within consecutive epochs have been investigated. This choice is motivated by the large differences in terms of camera type, radiometric content and snow cover between datasets reported in Table 1. In fact, including all available blocks in a unique project would result in a heavy processing burden, while the large differences in the image content would result in a failure of the MSfM;
3. a set of GCPs have been measured in photos from all available epochs and used for *datum* setup in the BBA; and alignment between each pair of dense point clouds obtained from MVS after MSfM has been refined by applying Iterative Closest Point (ICP – see Pomerleau at al., 2013 for a review) on some well distributed Stable Areas (SA) outside the glaciers, as proposed in Scaioni at al. (2023). Point clouds generated in these SAs are also used for quality assessment, which is based on M3C2 (Multi-scale Model to Model – Lague et al., 2013) technique implemented in CloudCompare ver. 2.13.1 “Kharkiv” software package (www.cloudcompare.org).

### 2.4 Comparison of point clouds

**2.4.1. Selection of Stable Areas.** Stable Areas are selected in locations where no significant changes are expected, such as on bare rock, low-vegetated areas, outcrops, etc. An innovative solution to help the detection of these Stable Areas consists in the use of the European Ground Motion Service (EGMS) data, which can be accessed through a public geoportal (https:// egms.land.copernicus.eu/). Here information about ground deformation is reported from 2015-2022, and continuously updated. Data are derived from processing of Sentinel-1 SAR images based on advanced InSAR techniques. The analysis of the region of Miage/Brenva Glaciers allows the location of those areas that remained stable, at least in the period covered by Sentinel-1 data. Here, Level 2 (namely “Calibrated”) Products of EGMS (Ferretti et al., 2021) from descending satellite orbit tracks have been exploited (as shown in Fig. 1), and then, the datapoints with $|\text{mean velocity}| \leq 0.5\ [\text{mm/y}]$ and temporal coherence $\geq 0.7$ have been masked out from the dataset. This subset of “stable” (due to low velocity) and “reliable” (due to high temporal coherence) datapoints are used to determine the SAs in two different formats: pointwise and polygon, which are shown in Figure 1.

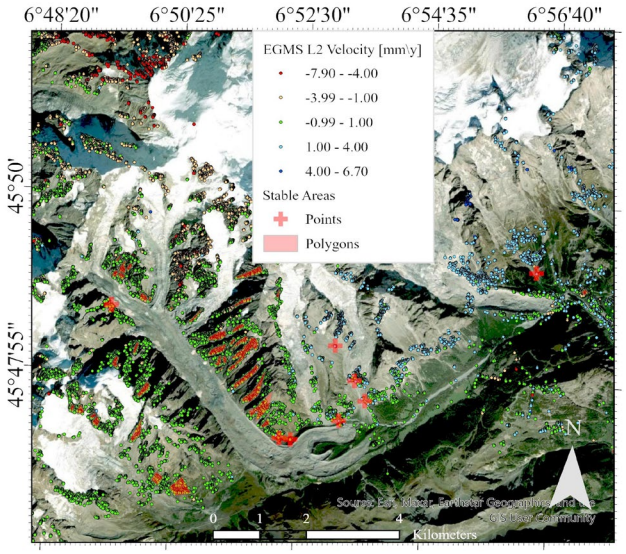


Figure 1. Location of the Miage Glacier with detected Stable Areas (SAs) according to EGMS (European Ground Motion Service) Level 2 product datapoints (background map from Google®).

**2.4.2. Change detection.** After assessment of point cloud quality and refinement of the coregistration, those portions falling in a polygon of the glacier outlines are compared by using the difference between volumes computed on a raster at both epochs to compare. The output consists in added, removed and total volumes, the latter used to generate deformation maps.

### 2.5 Experimental results aerial image processing

**2.5.1 Dataset selection.** MSfM is applied to each pair of consecutive epochs, to obtain two dense point cloud with a preliminary alignment, to be refined using ICP. In this analysis, photogrammetric blocks recorded at shorter time lapse have not been included in the analysis (i.e., 1956, 1983, 2001); consequently, relative changes occurred within consecutive epochs have been investigated. While the process to derive and compare dense point clouds has been applied to the entire region, the comparison is applied here only to the Miage Glacier.

**2.5.2 GCP.** A set of 10 GCPs has been derived from digital maps published online on the Geoportal of regional administration (https://mappe.regione.vda.it/pub/geoCartoSCT). Some details of buildings, boulders and other stable objects present in as many photos as possible was selected as GCPs (see a few examples in Fig. 2). Their corresponding image coordinates have been measured in photos from all available epochs and used in the BBA. An accuracy of ±10 m has been adopted for weighting GCP observations. GCPs played an important role to mitigate a bias between dense point clouds obtained from consecutive blocks.

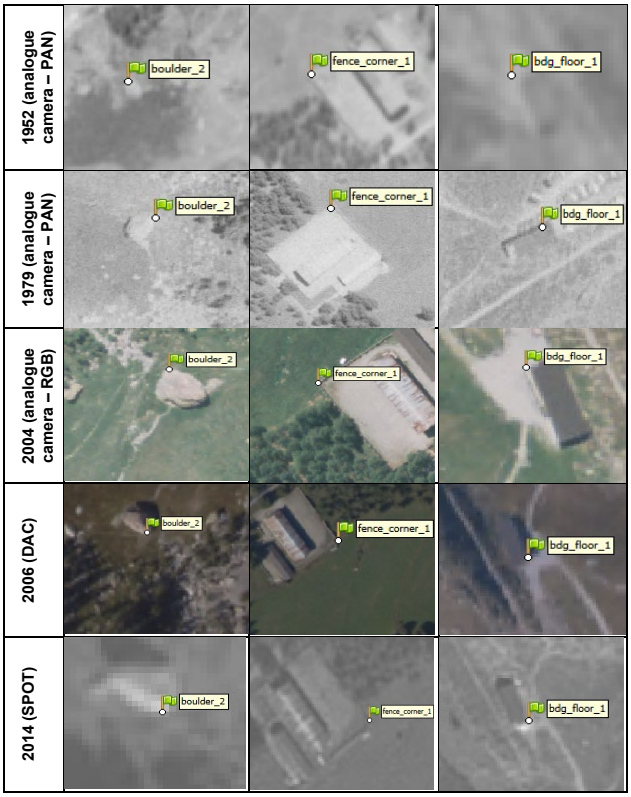


Figure 2. A few examples of ground control points (GCPs) measured in different images.

**2.5.3. MSfM.** The application of MSfM following the workflow described at paragraph 2.3.1 has been done per each couple of consecutive epochs (see Table 2). The accuracy level “Very High” has been selected in all projects to maximize the quality of image orientation. An initial step has been run by considering each block independently and by measuring GCPs. This stage has been focused to check the presence of problems. For instance, some epochs include photos acquired in different ways or at different altitude (e.g., in the blocks from 1988 and 1996).
The selection of a homogeneous subset resulted in better results in term of quality of the dense point cloud. In addition, this stage was also used to compute camera inner orientation and calibration parameters. When all or a part of these parameters were available from a calibration certificate or from the photos’ border, these values have been constrained. In other cases, they have been estimated during BBA. With a few exceptions, only the principal distance and two coefficients for radial symmetric distortion in the Brown model were estimated, given the high quality of analogue photogrammetric cameras (Kraus, 2008). In a second stage, independent datasets were merged to prepare MSfM projects, each of them comprehending images from two consecutive epochs and GCP coordinates.

| Epochs | #adopted images (epochs 1 / 2) | # TPs | Avg. rays/ TP | Avg. #TP per image | Avg. error on TPs [pix] | Fraction of TPs per epoch [%] | | | # GCPs | 3D residuals on GCPs | |
|---|---|---|---|---|---|---|---|---|---|---|---|
| | | | | | | TPs in Epoch 1 | TPs in Epoch 2 | Inter-epoch TPs | | Ground [m] | Images [pix] |
| ***1952-1958*** | 33 / 20 | 58198 | 2.77 | 3875 | 1.13 | 56.1 | 41.5 | 2.5 | 7 | 11.1 | 5.91 |
| ***1958-1967*** | 20 / 15 | 40676 | 2.43 | 2468 | 0.97 | 51.9 | 48.0 | 0.1 | 7 | 10.1 | 4.43 |
| ***1967-1979*** | 15 / 14 | 32147 | 2.31 | 2080 | 0.91 | 72.0 | 28.0 | 0.0 | 8 | 10.4 | 4.91 |
| ***1979-1988*** | 14 / 21 | 30848 | 2.37 | 1870 | 2.90 | 28.3 | 66.4 | 5.3 | 10 | 13.3 | 13.01 |
| ***1988-1996*** | 21 / 10 | 31474 | 2.38 | 2694 | 1.56 | 35.8 | 64.0 | 0.2 | 7 | 14.5 | 11.73 |
| ***1996-2000*** | 10 / 24 | 39593 | 2.37 | 3055 | 1.12 | 84.0 | 13.1 | 2.8 | 10 | 53.5 | 6.43 |
| ***2000-2004*** | 23 / 12 | 40229 | 2.51 | 2790 | 0.71 | 39.3 | 60.5 | 0.2 | 10 | 8.5 | 8.77 |
| ***2004-2006*** | 12 / 23 | 48931 | 2.78 | 3650 | 0.43 | 28.2 | 70.7 | 1.1 | 10 | 3.6 | 2.60 |

Table 2. Properties of photogrammetric datasets from online repositories (DAC: digital aerial camera; PAN: panchromatic photos; RGB: colour photos).

Some indicators of the quality of BBA input and output are reported in Table 2.
Different blocks have shown similar results in term of extracted tie points (TPs). While the total number of TPs and the average number per image are always more than sufficient, the multiplicity is quite low, indicating that TPs have not been measured in many images. But the more critical outcome concerns the low fraction of TPs measured between different epochs, which is always below 5.3%. About residuals on GCPs, their values may be generally accepted considering the difficulty in their measurement in some images (see examples in Fig. 2) and the uncertainty of their ground coordinates (estimated as ±10 m) due to their derivation from a digital map. A direct measurement of these GCPs in the field by using GNSS sensors would benefit the image orientation.
These results are motivated by the weak geometry of the adopted blocks, which are part of larger datasets and, when merged between different epochs, may show poor overlap and uneven photo scales (see Table 1). As described in Subsection 2.7, when photogrammetric points are compared in SAs, the discrepancies will be too high and will require further refinement at a later stage.

**2.5.4. Generation of dense point clouds**. The last step of photogrammetric processing consists in the generation of a dense point cloud from each block based on the exterior orientation and camera calibration parameters computed from each MSfM project. This task has been carried out using MVS matching implemented in AMP. The “High” quality level and the “moderate” filtering have been selected. An additional filtering is applied before moving to the change detection analysis, based on removing those points at a distance larger than 2 times the standard deviation computed in a neighbour of 10 points. In some cases (e.g., 1996 and 2000), the point cloud ended up being quite noisy or presented some duplicated surfaces. These problems have been partially coped with the exclusion of some photos from MVS matching and by manual editing. Since the focus here is on the tongue of the Miage Glacier, each point cloud has been segmented in a wider region around it, as shown in Figure 3. In Table 3, the number of points in the tongue per each epoch are reported.

### 2.6 Photogrammetric processing of Very-High-Resolution Images (VHRI)

Processing of the SPOT 6 satellite stereo pair collected over the Miage/Brenva Glaciers on 27th September 2014 was carried out in AMP as for the aerial imagery. In the case of SPOT 6, the orientation parameters are extracted from the Rational Polynomial Functions (RPC) provided with the images. The stereo pair was processed through a two-step workflow, including the refinement of image registration first (including 10 GCPs that could be identified in SPOT 6 images) and dense matching. These tasks were computed at “Very High” and “High” accuracy levels in AMP, which involved the use of images at their full resolution without down-sampling. A total number of 3834 tie points were extracted from the images, with an average reprojection error of 0.16 pixels.
Thanks to the estimated RPC, it was possible to derive a dense point cloud from the SPOT 6 stereo pair, consisting of 20.7M points which cover an area of approximately 150 km$^2$ (Fig. 3).

### 2.7 Assessment and coregistration refinement of point clouds

A total of ten point-clouds have been generated from aerial and satellite imagery. This have been first validated by using some SAs around the tongue of the Miage Glacier (see Fig. 3).

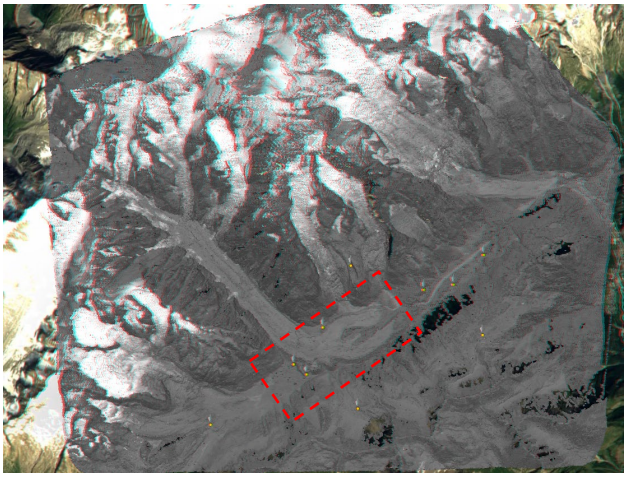

Figure 3. Reconstructed dense point cloud from SPOT 6 stereo images (in grey values display); yellow points represent GCPs. The red rectangle contains the SAs around the tongue of Miage Glacier adopted for quality assessment and co-registration refinement of point clouds.

These areas have been selected based on the analysis of EGMS Level 2 product datapoints and by considering morphological characteristics. An example of one point cloud of the tongue is shown in the bottom row of Figure 4.
Inside SA, each pair of consecutive point clouds were analysed and post-processed following the method described at Paragraph 2.3.2. In general, the coregistration based on ICP has introduced corrections in terms of 3D shift in the order of a few decades of metres, witnessing the poor quality of georeferencing obtained from MSfM. Residuals after ICP have been estimated with M3C2 technique. Since SAs also contain vegetation and other changed objects that may influence this analysis, statistics reported on the rightmost column of Table 3 have been computed after blunder filtering from residuals. These results give an estimated of the quality of each dataset, at least as far as its georeferencing is concerned.

### 2.8 Results of change detection analysis

The analysis of changes in the tongue of the Miage Glacier has been carried out by computing the differences of volume between point clouds obtained from consecutive epochs. This task has been done using the specific function in CloudCompare ver. 2.13.1. Point clouds have been rasterized according to a cell size of 5 m, which has been empirically decided after some preliminary tests. The vertical direction has been chosen, for computing volumes, since the tongue is quite flat. The results are reported in terms of nine deformation maps (Fig. 4) and parameters in Table 3. The results of M3C2 validation in SAs around the glaciers can be used as measure for the level of reliability of volume change and the average height difference.
Looking at the maps, we noticed different important patterns. The formation of fractures, crevasses and cavities gives a great contribution to the volumetric change. In most cases, positive changes are due to the ice flow from the accumulation areas and are compensated by an initial loss. On the other hand, the ablation of the upper surface is a quite common process in the Miage Glacier, which also resulted in the formation of supraglacial ponds (Tinti et al., 1999; Stefaniak et al., 2021). On the other hand, while in the latest analysed period (from 2004 to 2012) the glacier lost an important volume of ice, the debris cover resulted in a protecting effect, which did not affect its extension (see Stefaniak et al., 2021)

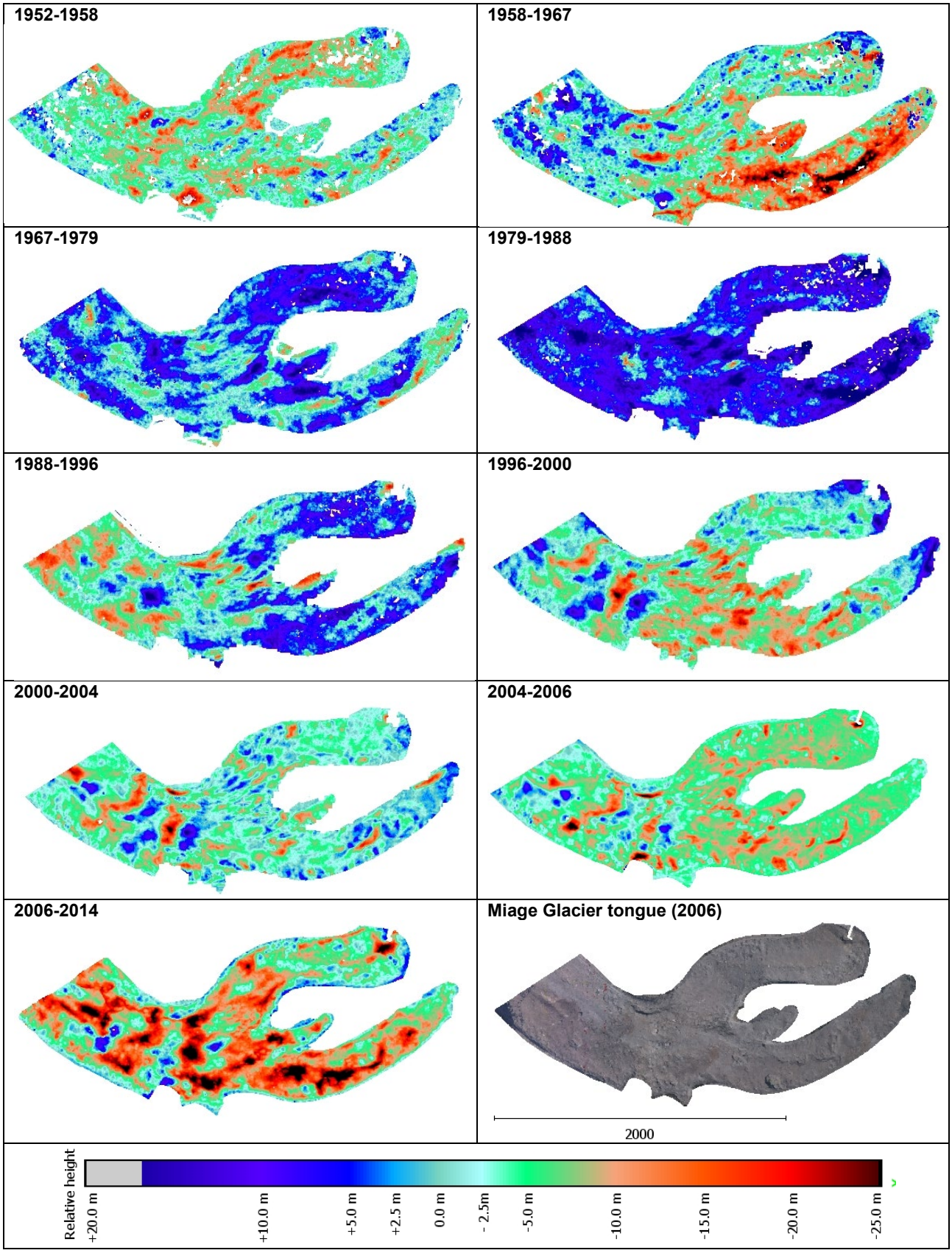


Figure 4. Maps depicting volume changes between consecutive epochs of the Miage Glacier tongue.

| epochs | # million points | | ΔT (months) | Area [Mm²] | Volumetric change | | | | | Analisys of M3C2 distances | | | |
|---|---|---|---|---|---|---|---|---|---|---|---|---|---|
| | epoch 1 | epoch 2 | | | accum. [Mm³] | melted [Mm³] | ΔV [Mm³] | Δh [m] | Δh/years [m/y] | mean [m] | std.dev. [m] | RMSE [m] | %valid data |
| ***1952-1958*** | 0.76 | 0.83 | 72 | 1.701 | 0.539 | 9.169 | -8.63 | -5.07 | -0.85 | -0.1 | 3.5 | 3.5 | 97.77 |
| ***1958-1967*** | 0.83 | 0.51 | 106 | 1.717 | 1.0334 | 13.141 | -12.108 | -7.05 | -0.80 | -0.3 | 7.3 | 7.3 | 89.44 |
| ***1967-1979*** | 0.51 | 1.16 | 143 | 1.829 | 6.928 | 2.139 | 4.789 | 2.62 | 0.22 | -0.2 | 5.6 | 5.6 | 93.90 |
| ***1979-1988*** | 1.16 | 1.02 | 107 | 1.785 | 15.413 | 0.271 | 15.142 | 8.48 | 0.95 | -0.4 | 5.5 | 5.5 | 97.09 |
| ***1988-1996*** | 1.02 | 0.55 | 96 | 1.700 | 4.309 | 4.976 | -0.667 | -0.39 | -0.05 | -0.7 | 5.8 | 5.9 | 92.78 |
| ***1996-2000*** | 0.55 | 0.64 | 48 | 1.833 | 1.662 | 9.224 | -7.562 | -4.13 | -1.03 | 0.8 | 7.4 | 7.4 | 90.12 |
| ***2000-2004*** | 0.64 | 2.04 | 48 | 1.846 | 1.071 | 6.566 | -5.495 | -2.98 | -0.74 | 0.3 | 5.4 | 5.5 | 93.98 |
| ***2004-2006*** | 2.04 | 0.69 | 24 | 1.859 | 0.149 | 13.227 | -13.078 | -7.03 | -3.52 | 1.1 | 5.8 | 5.9 | 97.46 |
| ***2006-2014*** | 0.69 | 0.20 | 97 | 1.859 | 0.242 | 19.106 | -18.864 | -10.15 | -1.26 | -1.0 | 4.6 | 4.7 | 97.85 |

Table 3. Results of change detection analysis on the terminus of Miage Glacier (RMSE: Root Mean Squared Error). The analysis of M3C2 distances is related to the area around the glacier; statistics have been computed after outlier rejection.

## 3. Snow-cover analysis

### 3.1 Data and method

**3.1.1 Data.** Optical satellite data at the medium-high spatial resolution, i.e., LANDSAT 5-TM (Thematic Mapper), LANDSAT 8/9-OLI/OLI2 (Operational Land Imager), and Sentinel 2-MSI (Multispectral Instrument), acquired in the period 1984-2023, have been used for studying the evolution of snow-cover of the Miage and Brenva Glaciers. The time-series of satellite imagery have been analysed by exploiting the high computational resources and the extended data archive of the Google Earth Engine (GEE) platform (Gorelick et al., 2017).

**3.1.2. Processing workflow.** A multi-temporal approach, mainly based on the use of the *Normalized Difference Snow Index* (NDSI - Dozier, 1989), is adopted to discriminate the different covers of the glaciers (e.g. ice, snow, debris). The advantage of using multitemporal approaches to analyse the spectral indices relies on the circumstance that a single date image may not be always sufficient to scrutinize between land covers based only on their spectral signatures (Jewell, 1989; Van Niel and Mc Vicar, 2004). For instance, Filizzola et al. (2018) exploited this concept to discriminate different vegetational land covers and introduced the spectral-temporal index called TeNDI (*temporal NDVI difference index*).
In this work, we propose an algorithm mainly based on the assumption that the different types of glacier cover may assume different values of the NDSI during the year. Looking at Figure 5, where the trends of the NDSI index (i.e., spectral-temporal signatures) computed by using Sentinel 2 imagery over two different locations of the glacier are reported, it is possible to note that the pixel located in the upper part of the glacier (blue line), and not contaminated by clouds, assume high values of NDSI during the whole year. On the other hand, the pixel located in the lower part of the glacier (red line) shows a drop of the NDSI index in the summer and the fall periods. These circumstances suggest that the pixels that have high values of the NDSI during the whole year are characterized by persistent snow cover, unlike those pixels where a drop of the NDSI occurs. Therefore, by comparing the NDSI values in different periods of the year (e.g., winter and summer), we expect to discriminate the persistent snow covers of the glacier from those that are not.
To emphasize these two different land covers of the glacier based on their spectral–temporal profiles, the TeNDIS (*Temporal Normalized Difference Index for Snow cover*) index was introduced:

$$TeNDIS(x, y, t_w, t_s) = NDSI_{MVC}(x, y, t_w) - NDSI_{MVC}(x, y, t_s) \quad (1)$$

where $NDSI_{MVC}$ is the Maximum Value Composite (MVC - Holben, 1986) of the NDSI for each pixel $(x,y)$ during the winter $t_w$ (i.e., January, February, and March) and summer $t_s$ (i.e., July, August and September) periods. It should be noted that the choice to use the maximum value composite of NDSI rather than a single date image has been considered to minimize residual cloud contamination and other possible effects due to different observational conditions (e.g., atmospheric transmittance, satellite view angle).

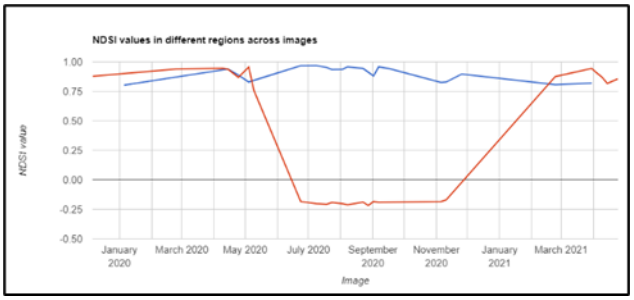


Figure 5. Spectral–temporal signatures of two different coversof a glacier. Blue line identifies a pixel located in the upper part of the glacier, while the red line shows pixel in the lower part.

TenDIS index has been implemented on LANDSAT and Sentinel 2 observations by following these steps:

1. *Top of Atmosphere* (TOA) images collected from January to March and from July to September in the period 1984-2023, which have a cloud coverage of less than 30%, have been selected from the data-sets available in the GEE catalogue;
2. by using standard cloud masks associated to TM, OLI/OLI 2 and MSI imagery, clear pixels have been discriminated from cloudy pixels;
3. per each clear sky pixel, the NDSI index has been computed by using the TOA reflectance measured in the green (~0.52 - 0.60 μm) and shortwave infrared (SWIR; ~ 1.55 - 1.75μm) bands;
4. per each year and each pixel of Miage and Brenva Glaciers, the TeNDI index has been computed based on Eq. (1); and
5. synthetic images representing the annual glacier cover have been generated and the yearly snow cover was mapped for both glaciers. The Otsu algorithm (Otsu, 1979) has been adopted for the automatic detection of the thresholds to be used to separate snow from no-snow areas.

### 3.2 Experimental results

Figure 6 shows a sequence of TeNDIS images based on S2-MSI observations for Miage and Brenva Glaciers from 2021 up to 2023. Here, in blue are represented the portions of the glacier characterized during the whole year by snow cover, whilst in orange are represented those portions of the glacier where the snow cover disappears during summertime. By comparing the maps of Figure 6, it is possible to note that for the Miage Glacier,

a significant reduction of the snow cover happens in 2022 in comparison with 2021 (see green circle in Fig. 6).
For a better overview of snow cover variations over a 40-year (1984-2023) period, in Figure 7 the temporal trends of the persistent snow cover are reported. For both glaciers under investigation, the fraction of the pixels classified as snow in TeNDIS images obtained using L5-TM and L8/9-OLI/OLI2 observations have been computed. The outlines of both glaciers have been derived from the glacier inventory for the entire Alps made by Paul et al. (2020). In this plot, only years where at least 95% of the pixels of the glacier are available for the computation of the TeNDIS index have been considered.

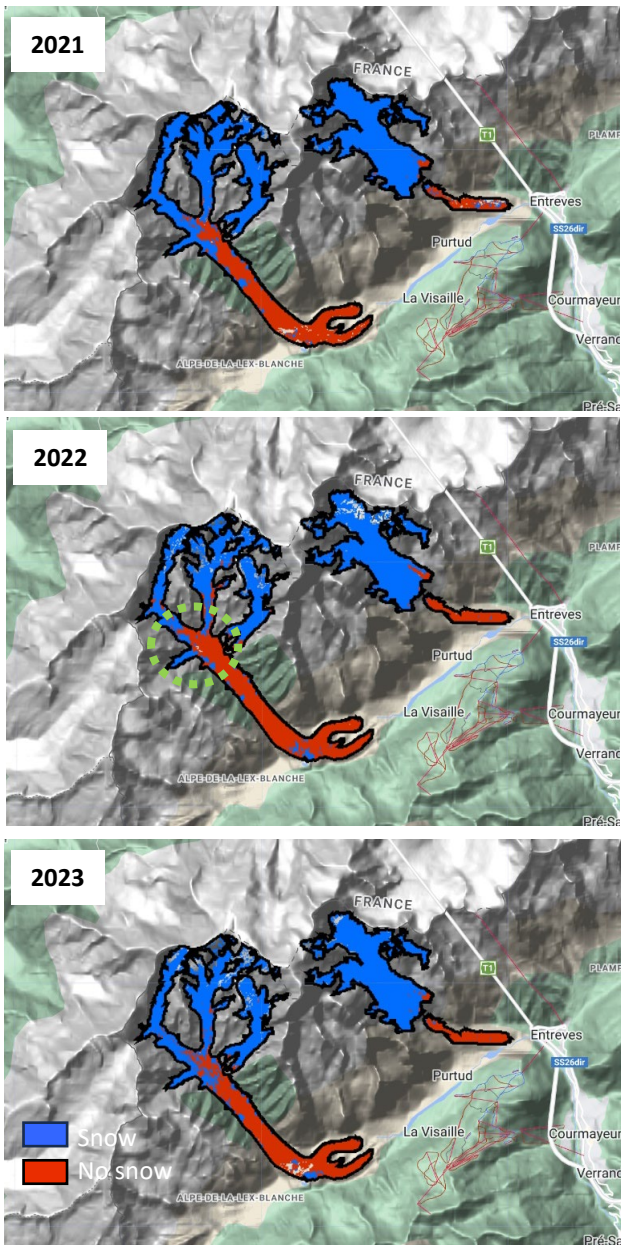


Figure 6. TeNDIS maps based on Sentinel 2-MSI observations for Miage and Brenva Glaciers. In blue are depicted the locations covered by a persistent snow cover, whilst in red those locations not affected by snow coverage during the whole year (background map from Google®).

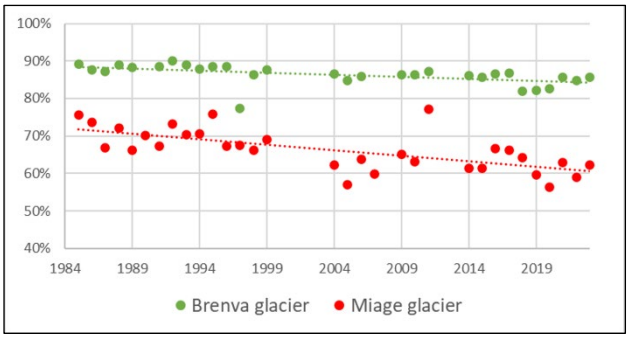


Figure 7. Trends of the persistent snow covers for Miage and Brenva Glaciers during 1984-2023 according to TeNDIS synthetic images based on LANDSAT 5-TM and LANDSAT 8/8- OLI/OLI2 observations.

## 4. Discussion

This study has involved the use of multiple data sources from remote sensing to assess the evolution of two glaciers in Mount Blanc Massif in Northern Italy. The adopted techniques allow to derive two main types of information: volume change and snow-cover. The latter are derived from the analysis of several data sets of archive aerial photos and satellite imagery dating back from 1952 to 2012.
Aerial blocks have been processed together for coregistration based on a technique called MSfM, followed by MVS matching for the generation of point clouds to be compared. From a technical point-of-view, the MSfM was not sufficient to obtain a good alignment between point clouds to compare, as already demonstrated in a Scaioni et al. (2023). On the other hand, a major effort in term of image pre-processing should be worth to be investigated in the future, to see whether the MSfM could provide better performances.
Results in terms of volumetric changes of Miage Glacier tongue shown in Figure 4 and Table 3 are coherent with the trend already reported by the scientific literature. We confirmed a period of positive mass gain between 1975 and 1991 (Diolaiuti et al., 2009), followed from 1990 by a phase of impressive decay , with formation of supraglacial ponds and ice cliffs (see Stefaniak et al., 2021).
In this work, we also introduced a multi-temporal/spectral approach for mapping glacier snow cover based on medium-high spatial resolution optical images. Aimed at understanding the spatial variability and the temporal trends of the snow cover of Miage and Brenva glaciers, we analyse about 40 years of satellite data, such as Landsat 5/8/9 and Sentinel 2 observations. Our findings highlight that both glaciers reduce year by year the area covered by snow persistently. Although the proposed method for mapping glacier snow cover needs to be validated by using independent observations and/or assessed by comparison with other approaches, the achieved results encourage us to improve our methodology, e.g. adopting more refined clouds masks rather than the standards cloud mask products and extend the analysis on other glaciers.
Looking at Figure 7, it is possible to note that both glaciers have a decreasing trend of the persistent snow cover. This means that every year both glaciers tend to reduce the area covered by persistent snow, and thus snow accumulation. This trend agrees with Stefaniak et al. (2021), which found an increase in the debris-cover extent from 1990-2018. This circumstance is more evident for the Miage Glacier (red dots in Fig. 7) rather than the Brenva Glacier (green dots in Fig. 7).

## 5. Conclusion and future work

This study has involved the use of multiple data source from remote sensing to assess the evolution of two glaciers in Mount Blanc Massif in Northern Italy. Here some technical methodologies and methods have been introduced and discussed, while more scientific results and their comparison will be expanded in future publications.
Based on archive aerial photos and satellite imagery (SPOT 6), the volume change of Miage Glacier was analysed in the period 1952-2014. The same approach proposed here will be extended to other glaciers in the region, while new satellite data could be included to investigate the later period from 2014 to date. This development would make it possible to overlap results in term of volumetric change with snow cover analysis, here analysed in the period 2021-2023, but likely applicable in the previous years.

## Acknowledgements

The authors would like to acknowledge the National Geographic and Forestry Institute of France and SwissTopo for delivering archive photos adopted in this study. Acknowledgements also go to the developers of CloudCompare open-source software.

## References

Diolaiuti, G., D’Agata, C., Meazza, A. Zanutta, A., Smiraglia, C., 2009: Recent (1975–2003) changes in the Miage debris-covered glacier tongue (Mont Blanc, Italy) from analysis of aerial photos and maps. *Geogr. Fis. E Din. Quat.* 32, 117-127.

Dozier, J., 1989: Spectral signature of alpine snow cover from the Landsat Thematic Mapper. *Remote Sens. Environ.* 28, 9-22.

Elias, M., Isfort, S., Eltner, A., Maas, H.-G., 2024: UAS Photogrammetry for Precise Digital Elevation Models of Complex Topography: A Strategy Guide. *ISPRS Ann. Photogramm. Remote Sens. Spatial Inf. Sci.*, X-2-2024, 57-64.

Filizzola, C., Corrado, R., Falconieri, A., Faruolo, M., Genzano, N., Lisi, M., Mazzeo, G., Paciello, R. Pergola, N., Tramutoli, V., 2018: On the use of temporal vegetation indices in support of eligibility controls for EU aids in agriculture. *Int. J. Remote Sens.* 39(14), 4572-4598.

Ferretti, A., Passera, E., Capes, R., 2021: Algorithm Theoretical Basis Document. EGMS Documentation, available online at URL: https://land.copernicus.eu/en/products/european-ground-motion-service/ (22nd July 2024).

Feurer, D., Vinatier, F., 2018: Joining multi-epoch archival aerial images in a single SfM block allows 3-D change detection with almost exclusively image information. *ISPRS J. Photogramm. Remote Sens.* 146, 495-506.

Genzano, N., Fugazza, D., Eskandari, R., Scaioni, M., 2024: Multitemporal Structure-from-Motion: A Flexible Tool to Cope with Aerial Blocks in Changing Mountain Environment. *Int. Arch. Photogramm. Remote Sens. Spatial Inf. Sci.*, XLVIII-2-2024, 99-106.

Gorelick, N., Hancher, M., Dixon, M., Ilyushchenko, S., Thau, D., Moore, R., 2017: Google Earth Engine: Planetary-scale geospatial analysis for everyone. *Remote Sens. Env.* 202, 18-27.

Holben, B.N., 1986: Characteristics of Maximum-Value Composite Images from Temporal AVHRR Data. *Int. J. Remote Sens.* 7, 1417-1434.

IGNF (National Geographic and Forestry Institute of France), 2024: Geoportal “IGN – Remontez le temps,” available online at URL: https://remonterletemps.ign.fr/ (22nd July 2024).

Jewell, N. 1989: An Evaluation of Multi-Date SPOT Data for Agriculture and Land Use Mapping in the United Kingdom. *Int. J. Remote Sens.* 10, 939-951.

James, M.R., Chandler, J.H., Eltner, A., Fraser, C., Miller, P.E., Mills, J.P., Noble, T., Robson, S., Lane, S.N., 2019: Guidelines on the use of structure-from-motion photogrammetry in geomorphic research. *Earth Surf. Process. Landforms* 44, 2081-2084.

Kraus, K., 2008. *Photogrammetry - Geometry from Images and Laser Scans*. Walter de Gruyter, Berlin (Germany).

Lague, D., Brodu, N., Leroux, J., 2013: Accurate 3D comparison of complex topography with terrestrial laser scanner: Application to the Rangitikei canyon (N-Z). *ISPRS J. Photogramm. Remote Sens.* 82, 10-26.

Lindenbergh, R., Pietrzyk, P., 2015: Change detection and deformation analysis using static and mobile laser scanning. *Appl. Geomatics* 7, 65-74.

Otsu, N., 1979: A threshold selection method from gray-level histograms. *IEEE Trans. Syst. Man. Cybern*. 9, 62-66.

Paul, F., Rastner, P., Azzoni, R.S., Diolaiuti, G., Fugazza, D., Le Bris, R., Nemec, J., Rabatel, A., Ramusovic, M., Schwaizer, G.,

Smiraglia, C., 2020: Glacier shrinkage in the Alps continues unabated as revealed by a new glacier inventory from Sentinel-2. *Earth Syst. Sci. Data* 12, 1805-1821.

Pomerleau, F., Colas, F., Siegwart, R., Magnenat, S., 2013: Comparing ICP variants on real-world data sets. *Autonom. Robots* 34, 133-148.

Racoviteanu, A.E., Williams, M.W., Barry, R.G. 2008: Optical Remote Sensing of Glacier Characteristics: A Review with Focus on the Himalaya. *Sensors* 8(5), 3355-3383.

Scaioni, M., Malekian, A., Fugazza, D., 2023: Techniques or Comparing Multi-Temporal Archive Aerial Imagery for Glacier Monitoring with Poor Ground Control. *Int. Arch. Photogramm. Remote Sens. Spatial Inf. Sci.*, XLVIII-M-1-2023, 293-300.

Stefaniak, A., Robson, B., Cook, S., Clutterbuck, B., Midgley, N., Labadz, J., 2021: Mass balance and surface evolution of the debris-covered Miage Glacier, 1990 – 2018. *Geomorphol.* 373, paper No. 107474.

SwissTopo, 2024. LUISS geoportal, available online at URL: https://map.geo.admin.ch/?topic=swisstopo&layers=ch.swisstopo.lubis-luftbilder_schraegaufnahmen,ch.swisstopo.lubis-luftbilder_farbe,ch.swisstopo.lubis-luftbilder_schwarzweiss&bgLayer=ch.swisstopo.pixelkarte-farbe&layers_timestamp=,99991231,99991231&catalogNodes=1392,1430&lang=it&layers_visibility=false,false,true (22nd July 2024).

Taylor, L.S., Quincey, D.J., Smith, M.W., Baumhoer, C.A., McMillan, M., Mansell, D.T., 2021: Remote sensing of the mountain cryosphere: Current capabilities and future opportunities for research. *Progr. Phys. Geog.: Earth Env.* 45(6), 931-964.

Tinti, S., Maramai, A., Cerutti, A.V., 1999: The Miage Glacier in the Valley of Aosta (Western Alps, Italy) and the extraordinary detachment which occurred on August 9, 1996. *Phys. Chem. Earth. A Solid Earth Geod.* 24(2), 157-161.

Van Niel, T.G., Mac Vicar, T.R., 2004: Determining Temporal Windows for Crop Dissemination with Remote Sensing: A Case Study in the South-Eastern Australia. *Comput. Electr. Agric.* 45, 91–108.